Indian Journal of Pure & Applied Physics
Vol. 62, June 2024, pp. 423-428
DOI: 10.56042/ijpap.v62i6.9146

Structural, Optical and Photocatalytic Properties of $SrTiO_3$ Perovskite obtained by Solvothermal Method

M Anbuvannan[a]*, V Maria Vinosel[b], P Dhatshanamurthi[c], M Ramesh[d] & S Uvarajan[a]

[a]Department of Physics, Thiruvalluvar University, Serkkadu, Vellore, Tamil Nadu 632 115, India

[b]Department of Physics, Sri Akilandeswari Women's College, Wandiwash, Tamil Nadu 604 408, India

[c]Department of chemistry, Sun Arts and Science College, Tiruvannamalai, Tamil Nadu 606 755, India

[d]Department of Physics, M.V. Muthiah Government Arts College for Women, Dindigul, Tamil Nadu 624 001, India

Received 28 February 2024; accepted 13 March 2024

The Solvothermal method was employed to produce bare TiO_2 nanoparticles and 5wt% $SrTiO_3$. The resultant samples were investigated using various instruments including X-ray diffraction (XRD), UV- Visible spectroscopy (UV), scanning electron microscopy (SEM), energy dispersive X-ray spectroscopy (EDX), and high-resolution transmission electron microscopy (HRTEM). The growth and crystallization of $SrTiO_3$ were analyzed using XRD. The SEM investigation revealed the spherical shape and aggregation of the nanoparticles, and the sample optical bandgap energy was found to be 3.2 eV. The maximal photodegradation efficiency of Congo red dye was achieved by the action of the valence band holes.

Keywords: Strontium titanate; Solvothermal; Structural; Morphology and photocatalytic activity

1 Introduction

Titanium dioxide (TiO_2) is a well-known and excellent photocatalyst for the treatment of organic dyes because of its photochemical stability, non-toxicity, insolubility, and low cost[1-3] TiO_2 is more active under UV irradiation because of its broad energy gap. Owing to the high recombination rate of photogenerated electrons and holes[4], and one of the most significant multifunctional perovskite materials is strontium titanate ($SrTiO_3$), an important n-type semiconductor with a band gap of approximately 3.2 eV[5-7]. It has several beneficial properties, including a high dielectric constant, good insulation[8], resistive oxygen gas sensors [9,10], solar cells[11], solid oxide electronic devices[12], catalytic, oxygen transport, ferroelectric, pyroelectric, piezoelectric, and the ability to be used as a substrate during the growth of thin-film perovskite compounds[13] as well as photocatalysts and photoelectrodes for water splitting. It is commonly known that the structure, shape, and size of nanoparticles affect their properties, in addition to their chemical makeup and production processes. Therefore, it is important to adjust the size and form of $SrTiO_3$ particles for both basic research and the creation of ceramics and composite materials with specific qualities. A variety of synthesis techniques have been used to produce both pure and doped $SrTiO_3$, including hydrothermal synthesis[14–16], solid-state reactions[17], the sol–gel method[18,19], the micro-emulsion approach[20], and the polymeric precursor method[21–23]. In this paper, we report the synthesis of $SrTiO_3$ using a solvothermal technique. The synthesized nanoparticles were studied using XRD, UV-Vis spectroscopy, SEM with EDAX, and HR-TEM to characterize the structure, optical properties, and morphology of $SrTiO_3$ nanoparticles. The photocatalytic properties of the samples for the removal of toxic pollutants were investigated. Congo red dye was used as a model pollutant and was degraded under visible light. Photocatalyst studies were more efficient; reaching a maximum after 60 minutes. Cui *et al.* [24] recently reported controlled homogeneity of the precursor in the synthesis of $SrTiO_3$ nanoparticles using an epoxide-assisted solvothermal method. In this study, a solvothermal process was successfully used to manufacture bare TiO_2, and 5wt% $SrTiO_3$ nanoparticles. The effect of reaction time on the nanotube size and shape was investigated. Additionally, research has been conducted on the photodegradation efficiency of Congo red dye of bare TiO_2, and 5wt% $SrTiO_3$ nanoparticles.

*Corresponding author:
(E-mail: anbuphy85@gmail.com)

2 Experimental

2.1 Preparation of SrO loaded TiO_2 Nanoparticle

SrO-loaded TiO_2 nanoparticles were synthesized by a solvothermal method. $Sr(NO_3)_2$, $C_{12}H_{28}O_4Ti$, $C_6H_8O_7$ and ethylene glycol (EG) were the main basic ingredients. First, an ethanol-diluted solution of tetra titanium (IV) isopropoxide was added to an aqueous solution of citric acid at pH 7, which was then corrected by adding an appropriate amount of ammonia. Solution I was a translucent yellowish liquid formed after 1 h of stirring at 80 °C. Simultaneously, deionized water was mixed with strontium nitrate dissolved in a 1:1 M ratio to create an aqueous solution, designated as solution II. Subsequently, solutions I and II were combined together. Simultaneously, ammonia was used to increase the pH to 7 until a translucent liquid was obtained. The solution was then heated to 80 °C under continuous stirred for six hours. The mixture was continuously stirred and citric acid was added. A stable, transparent sol was created after three hours of continuous stirring on a magnetic hot-plate stirrer, which progressively increased the viscosity of the solution. The molar ratio of the metal nitrate to citric acid was 1:4. A gel formed when it was continuously heated to approximately 110 °C. The viscous gel was then dried by continuous heating and stirring. The metal precursors and citric acid gel demonstrated self-propagating combustion behaviour, with the combustion process occurring in a matter of seconds. To obtain the nanocrystalline powders, drying the powders at 250 °C for two hours and then annealing them in a muffle furnace at 900 °C for 5 hours was done in the resulting powders.

2.2 Material characterization

The structural characteristics of bare TiO_2 and 5wt% $SrTiO_3$ nanoparticles were identified using powder X-ray diffraction (XRD). An X-ray diffractometer (Shimadzu-6000) was used to record the XRD patterns using Cu-Kα radiation (λ = 1.5406 Å). The UV- Visible spectroscopy recorded in the UV200101E model in the wavelength range of 200–800 nm. Using a scanning electron microscope equipped with an EDAX instrument (JEOL JSM – IT 200), the investigation was conducted to examine the surface morphology and elemental composition of $SrTiO_3$ nanoparticles. Transmission electron microscopy (TEM; JEM-2100) was used to assess sample morphology.

3 Results and Discussion

3.1 XRD analysis

The powder diffraction method is helpful for both quantitative and qualitative investigations, including phase fraction and lattice parameter measurement. The unit cell size, form, and translational symmetry, that is, the locations of the atoms relative to their peak intensities, were revealed by the diffraction pattern produced by this method. If the size is smaller than approximately 100–200 nm, it also provides information on the deviation from the ideal particle, as well as extended flaws and micro strain from the peak forms and width. The XRD patterns of the TiO_2 nanoparticles in the anatase phase of TiO_2 matched the XRD peaks. Fig. 1 displays the anatase phase TiO_2 (JCPDS 89-4921) diffraction peaks (101), (1 12), (200), (105), (204), (116), (220), and (215), corresponding to the distinctive peaks of TiO_2 at 25.3, 37.8, 48.0, 53.9, 62.7, 68.8, 70.3, and 75.1.

The cubic perovskite structure of the sample under study is the preferred index for its crystalline phase. $SrTiO_3$, the XRD pattern is in agreement with (JPCDS No.35-0734). Nevertheless, thorough analysis revealed that the crystalline phase of the produced particles appears to be best categorized as a cubic perovskite structure. Using the Debye–Scherrer equation, the grain size of the nanoparticles can also be determined from the diffraction peaks.

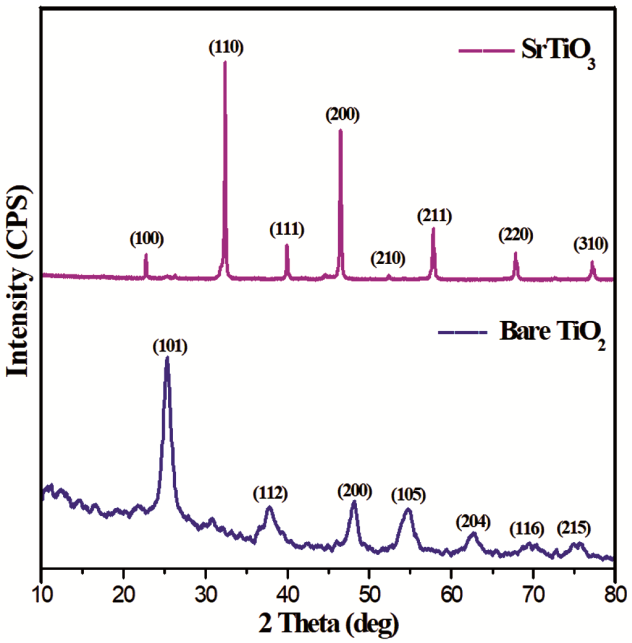

Fig. 1 — XRD Pattern of the as-prepared sample

$$D = \frac{K\lambda}{\beta Cos\theta} \text{ Å} \quad \text{... (1)}$$

where β is the full width at half maximum (FWHM) of the XRD peak, θ is the Bragg angle, D is the average particle size, K is the shape factor, and λ is the wavelength of the X-rays employed. The Scherrer equation predicts that the peaks become broader as particle size decreases. Based on the XRD results the (110) plane of $SrTiO_3$ was identified as a peak at 2θ = 32°. The other peaks at 2θ = 32.43°, 40.05°, 46.48°, 58.03°, 67.95°, and 72.28° corresponded to the $SrTiO_3$ structure (110), (111), (200), (211), (220), and (310) crystalline planes, respectively. The absence of any other phase peaks suggests that the $SrTiO_3$ nanoparticles were highly pure and exhibited good crystallinity. Based on the XRD results, the (110) plane of $SrTiO_3$ was identified as the peak at 2θ = 32°.The other peaks at 2θ = 32.43°, 40.05°, 46.48°, 58.03°, 67.95° and 72.28° correspond to the $SrTiO_3$ structure (110), (111), (200), (211), (220) and (310) crystalline planes, respectively. The absence of any other phase peaks suggests that the $SrTiO_3$ nanoparticles were highly pure and had good crystallinity. The bare TiO_2 crystallite size was 15.2 nm and the $SrTiO_3$ average crystallite size was 43 nm.

3.2 UV-Visible spectrum analysis

The UV-visible spectra of room-temperature bare TiO_2 and 5wt% $SrTiO_3$ nanoparticles, spanning from 200 to 800 nm, are depicted in Fig. 2(a). This spectrum was used to obtain more information regarding the electrical structure and quality of the nanoparticles.

The following formula relates the optical energy bandgap to both the absorbance and the photon energy in the high-energy portion of the absorption curve:

$$E_g = \frac{hc}{\lambda} \text{ eV} \quad \text{... (2)}$$

where h is Planck's constant (6.626 x 10^{-34}Js), C is the light velocity (3 x 10^8 m/s), λ is the wavelength (nm), and Eg is the bandgap energy (eV). The band gap energy of bare TiO_2 and 5wt% $SrTiO_3$ was found to be 3.2 eV, because $SrTiO_3$ is a pure white crystalline powder, and there are no obvious range absorption peaks in the powder. The excitonic absorption peak was proposed to be at 320 nm.

The Tauc plot of $(\alpha h\nu)^2$ versus the photon energy hν is shown in Fig. 2(b). Plotting $[\alpha h\nu]^2$ vs. hν and extrapolating the linear sections yields 3.2 eV. Eg values for $SrTiO_3$ nanoparticles. An optical density $(\alpha h\nu)^2$ vs. energy (E) plot was used to evaluate the optical bandgap of $SrTiO_3$. The direct bandgap of $SrTiO_3$ nanoparticles was calculated to be 3.2 eV, which is consistent with other reports in the literature.

3.3 SEM Analysis

The surface structures of the samples were investigated by SEM. Fig. 3(a) shows the results of the morphology research on $SrTiO_3$ nanoparticles. The resultant nanoparticles had a spherical form and some agglomeration, similar to the grains. Furthermore, Fig. 3(b) shows the EDAX analysis of $SrTiO_3$ NPs with 47.57% Sr, 28.68% Ti, and 23.75% oxides, which confirms the elemental composition of the $SrTiO_3$ nanoparticles[25].

3.4 HRTEM Analysis

High-resolution transmission electron microscopy (HRTEM) can be used to image individual crystallites. TEM enables the observation of crystallite ordering in secondary structures, in addition to examining the morphology of the individual crystallites. Using a 200 kV field emission

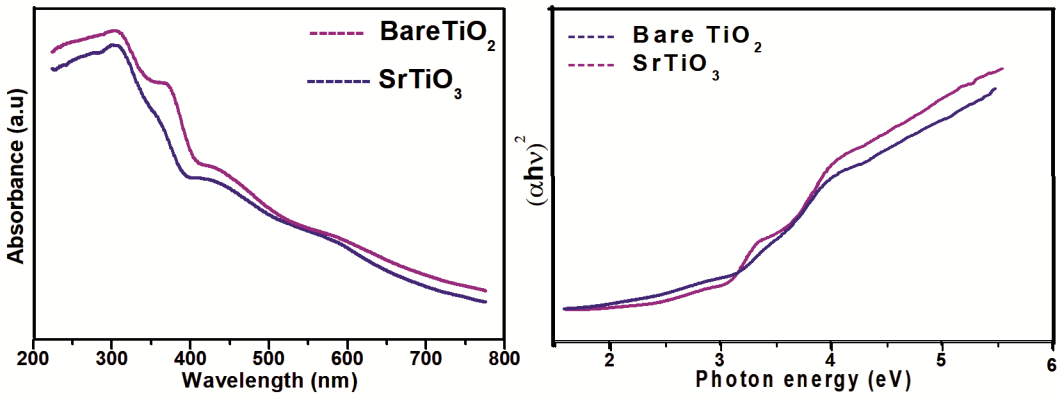

Fig. 2 — (a) UV-Vis spectra of as-prepared samples (b) Tauc plot for as-prepared samples

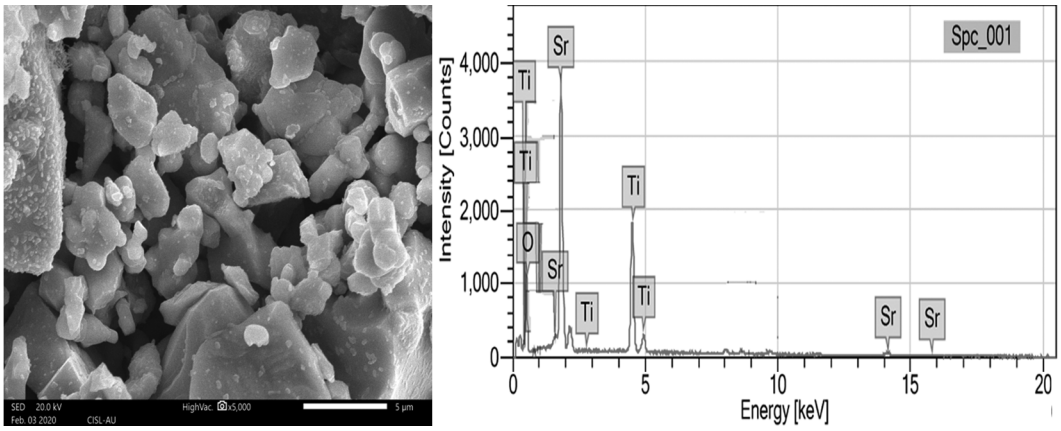

Fig. 3 — (a,b) SEM -EDAX pattern of $SrTiO_3$ nanoparticles

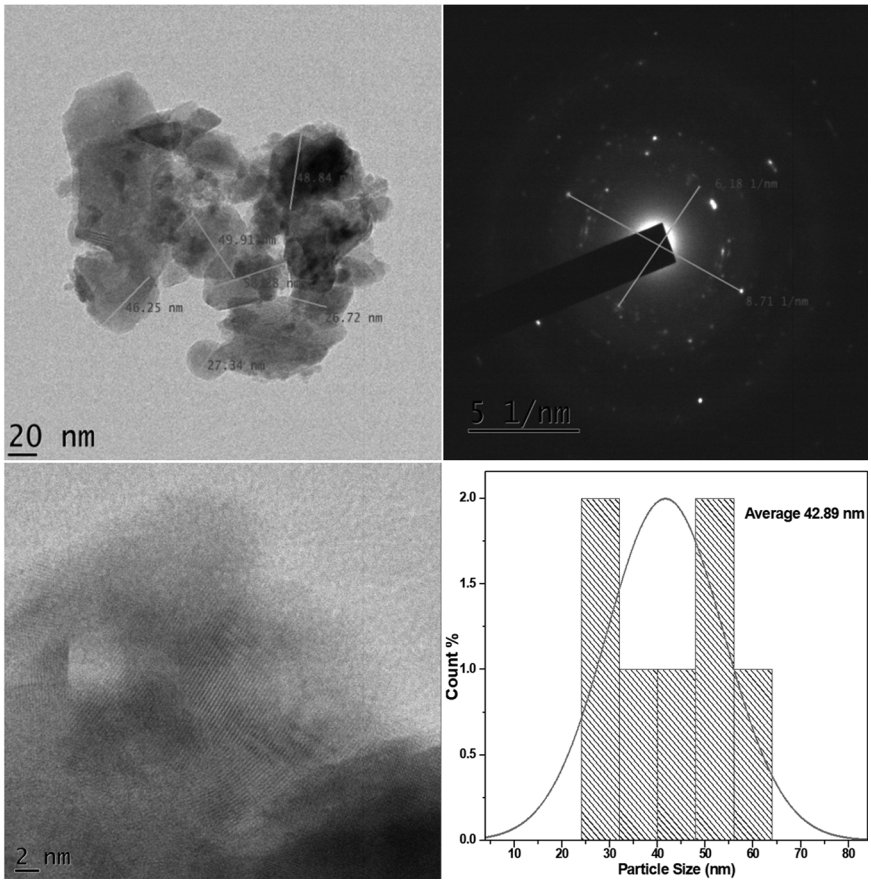

Fig. 4 — (a) TEM image (b) SAED pattern (c) HRTEM (d) Particle size histogram of $SrTiO_3$ nanoparticles

gun microscope, high resolution transmission electron microscopy was used to examine the size, shape, and crystallinity of the as-prepared and treated particles. Fig. 4 displays the images and related SAED pattern obtained from high-resolution transmission electron microscopy (HRTEM) used to characterize the morphology of the as-prepared $SrTiO_3$ nanoparticles.$SrTiO_3$ nanoparticles have a somewhat spherical form and mild aggregation. This demonstrates the polycrystalline nature of the nanoparticles produced. Each particle ranged in size from 50 to 20 nm. The particle sizes estimated from the XRD patterns and observed results were roughly in agreement.

3.5 Photodegradability of Congo red

The photodegradability of Congo red under UV irradiation using various photocatalysts is shown in

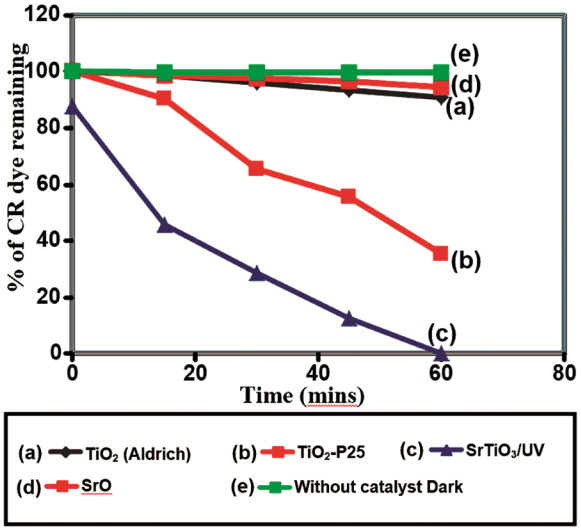

Fig. 5 — Photodegradability of Congo red: [CR] = 1×10^{-4} M, pH = 7, catalyst suspended = 3 g L^{-1}, airflow rate = 8.1 mL s^{-1}, I_{UV}= 1.381×10^{-6}einstein L^{-1} s^{-1}

Time	TiO_2 (Aldrich)	TiO2-P25	$SrTiO_3$	SrO	Without catalyst Dark
0	100	100	87.98	100	100
15	98.768	90.56	45.76	98.67	99.87
30	96.23	65.46	28.56	97.56	99.82
45	93.678	55.45	12.54	96.45	99.79
60	90.967	35.56	0	94.65	99.67

Fig. 5. When $SrTiO_3$ was exposed to UV light for 60 min, the dye completely degraded (curve c). The same experiment using TiO_2-P25 in the presence of UV light resulted in a 34.9% decrease in the dye concentration (curve b).

Based on these findings, it can be concluded that both UV light and the catalyst are required for the efficient degradation of the CR dye. Under the same conditions, the degradation percentages were 9.1% (curve a), 5.4 (curve d), and 1.6 (curve e) when bare TiO_2, SrO, and no catalyst were used, respectively. This demonstrates that $SrTiO_3$ is a more effective catalyst for CR degradation than other catalysts given table below.

Given the effectiveness of $SrTiO_3$ degradation, an investigation into the effects of the operating parameters was conducted to determine the ideal circumstances[26-28].

Mechanism

Scheme 1 illustrates the mechanism of charge separation and the photocatalytic reaction of the SrO-TiO_2 composite photocatalyst.The SrO and TiO_2

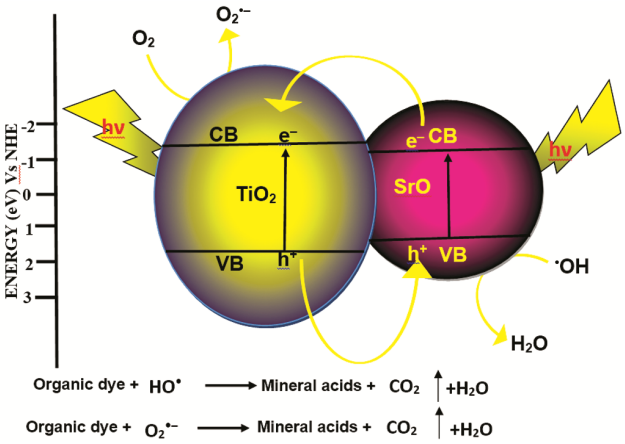

Scheme 1

band energy levels a expressed in relation to the NHE. The conduction band of SrO was somewhat lower than that of TiO_2, according to the photocatalytic process of the composite. An electron from the valence band of a semiconductor (TiO_2) that is exposed to UV radiation transitions to the conduction band, leaving a hole in the valence band. The reverse reaction between the photogenerated charge carriers is anticipated to be slowed by the injection of electrons from the conduction band of TiO_2 into the BaO particles, as shown by the photoelectron data. The transfer of electrons from the CB of TiO_2 to the CB of SrO occurs because of the UV radiation. An explanation of the charge separation mechanism and TiO_2 is that this electron transfer mechanism proceeds more quickly than electron-hole recombination. The dye is degraded by the increased production of $O_2^{\cdot-}$ (super oxide radical anion) by the electrons in the TiO_2 CB. After being photo excited by the UV light irradiation, the holes in SrO and those created in TiO_2 react with H_2O and OH^- to form $^{\cdot}OH$ (hydroxyl radicals), which are required to degrade the dye[29-32].

4 Conclusion

The fabrication of bare TiO_2 nanoparticles and 5wt% $SrTiO_3$ nanoparticles using a solvothermal process was the main goal of this project. The structural, morphological, and optical characteristics of the prepared samples were then characterized. The formation of cubic $SrTiO_3$ nanoparticles with an average crystallite size of 43 nm was confirmed using XRD datathe spherical shape and aggregation of the nanoparticles were revealed using SEM analysis. The EDAX spectrum confirms the elemental composition of the $SrTiO_3$ nanoparticles.The HRTEM image

shows uniformly sized spherical nanoparticles.The optical bandgap energy of the sample was found to be 3.2 eV. Future research may observe differences in particle size and shape due to variations in dopants and surfactants. The photocatalytic activity of $SrTiO_3$ nanoparticles is more efficient at degrading materials than other catalysts.

Acknowledgement

The authors are thankful and grateful to Department of Physics, Thiruvalluvar University, Serkkadu, Vellore -632115, Tamil Nadu, India, for providing all necessary facilities to carry out the present work successful.

References

1 Krishnakumar B & Swaminathan M, *J Mol Catal A: Chem,* 350 (2011) 16.
2 Wenjun D, Xiaoyun L, Jie Y, Wanchun G, Bingjie L, Chaorong L, Jianjun S & Ge W, *Mater Lett,* 67 (2012) 131.
3 Velmurugan R & Swaminathan M, *Res Chem Intermed,* 41 (2015) 1227.
4 Subash B, Krishnakumar B, Pandiyan V, Swaminathan M & Shanthi M, *Sep Purif Technol,* 96 (2012) 204.
5 Cardona M, *Phys Rev*, 140 (1965) 651.
6 SilvaaL F d, Maia L J Q, BernardiM I B, Andrés J A & Mastelaro V R, *Mater Chem Phys,* 125 (2011) 168.
7 Xian T, Yang H, Dai J F , Wei Z Q, Ma J Y, Feng W J, *Mater Lett,* 65 (2011) 3254.
8 Haeni J H, Irvin P, Chang W, Uecker R, Reiche P, Li Y L, Choudhury S, Tian W, Hawley M E, Craigo B & Tagantsev A K , *Nature*, 430 (2004) 758.
9 Hu Y, Tan O K, Pan J S, Huang H & Cao W, *Sens Acta B: Chem,* 108 (2005) 244.
10 Hara T & Ishiguro T, *Sen Acta B: Chem,* 136 (2009) 489.
11 Burnside S, Moser J E, Brooks K, Grätzel M & Cahen D, *The J Phys Chem B*, 103 (1999) 9328.
12 Pellegrino L, Pallecchi I, Marre D, Bellingeri E & Siri A S, *Appl Phys Lett,* 81 (2002) 3849.
13 Moreira M L, Andres J, Longo V M, Li M S, Varela J A & Longo E, *Chem Phys Lett*, 473 (2009) 293.
14 Um M H & Kumazawa H, *J Mater Sci,* 35 (2000) 1295.
15 Zhang S, Liu J, Han Y, Chen B & Li X, *Mater Sci Eng: B*, 110 (2004) 11.
16 Nyutu E K, Chen C H, Dutta P K & Suib S L, *The J Phys Chem C*, 112 (2008) 9659.
17 Tagawa H & Igarashi K, *J Am Ceram Soc,* 69 (1986) 310.
18 Trepakov V A, Savinov M E, Okhay O, Tkach A, Vilarinho P M, Kholkin A L, Gregora I & Jastrabik L*, J Eur Ceram Soc*, 27 (2007) 3705.
19 Pfaff G, *J Mater Chem,* 3 (1993) 721.
20 Pang Q, Shi J & Gong M, *J Am Ceram Soc*, 90 (2007) 3943.
21 Leite E R, Varela J A, Longo E & Paskocimas C A*, Ceram Int J,* 21 (1995) 153.
22 Zanetti S M, Longo E, Varela J A & Leite E R, *Mater Lett*, 31 (1997) 173.
23 Chang C H & Shen Y H, *Mater Lett,* 60 (2006) 129.
24 Cui H, Zayat M & Levy D, *J Non-Cryst Sol*, 353 (2007) 1011.
25 Kiran K S, Shashanka R & Lokesh SV, *Topics Catal,* (2022) 1.
26 Subash B, Krishnakumar B, Velmurugan R & Swaminathan M*, Sep Purif Technol*, 101 (2012) 98.
27 Subash B, Krishnakumar B, Swaminathan M, Shanthi M, *J Mol Catal A: Chem*, 366 (2013) 54.
28 Krishnakumar B & Swaminathan M, *Indian J Chem Sect A*, 49 (2010) 1035.
29 Krishnakumar B, Imae T, Miras J & Esquena J*, Sep Purif Technol*, 132 (2014) 281.
30 Grabowska E, Marchelek M, Klimczuk T, Lisowski W, Zaleska-Medynska A, *J Catal*, 350 (2017)159.
31 Keerthana S P, Yuvakkumar R, Ravi G, Thambidurai M, Nguyen H D & Velauthapillai D, *RSC Adv,* 13 (2023) 18779.
32 Anandhakumari G, Jayabal P, Balasankar A, Ramasundaram S, Oh TH, Aruchamy K, Kallem P & Polisetti V, *Heliyon*, 9 (2023) e20824.